6 Heat transfer - Experimental results

In this chapter we will present the results from the space experiment concerning heat transfer in critical systems. We will start by giving a general impression of the space experiment before attention is given to some specific analysis features. The subsequent detailed presentation of the results is divided into three main subjects: the quantitative understanding of the PE, the measurement of the thermal diffusivity and the determination of the specific heat at constant volume utilizing the PE.

6.1 General results

6.1.1 Experimental scenario

The actual experimental temperature scenario was as follows. The sample was first heated to $T - T_c \approx 2500$ mK (48 ˚C) at which appreciable time (>2 hrs) was allowed for it to reach thermal equilibrium (i.e. become homogeneous). It was then cooled in steps to 1025, 325, 125, 45 and finally 15 mK above T_c. At T_c + 15 mK, a cooling ramp at a rate of 13.333 mK/hr was initialized and maintained until the crossing of T_c was confirmed by observation of phase separation. The sample was again homogenized at $T - T_c \approx 2500$ mK and cooled, in steps, to 2000, 1500 and 800 mK above T_c and then, in ramps, to 450, 150, 50, 30, 10, 5, 2 and 1 mK above T_c. Finally, the sample was heated slowly to T_c + 100 mK to check for hysteresis effects.

Following each change in temperature, various waiting periods were employed in an attempt to improve approximate thermodynamic equilibrium. However, the IF images indicated that true equilibrium was never reached, but that with specific precautions a ‘quasi-steady state’ could be achieved within reasonable time, e.g. at $T - T_c = 1$ mK in 3 hours and after approaching with a slow ramp (2 mK/hr). The fluid was considered to be in a ‘quasi-steady state’ when the density changes were decreased to a degree that the fringes in the interferograms moved significantly less than their typical movement following local heating of the fluid. During the mission this was checked by the set up in the DUC.

When, at a set temperature, a steady state was obtained, constant-current heating pulses were applied to the fluid by the plate heater. The power delivered to the system by the plate heater varied between 1 and 200 µW (corresponding to approximately 5 mW/m^2 and 1 W/m^2 respectively at the heater[†]) and the pulse duration was varied between 1 and 5 minutes.

6.1.2 The critical temperature

The apparent critical temperature, on the scale indicated by the measurement thermistor, was determined at the time of filling which was several months before the mission. For several reasons, it was appropriate to verify this value during the actual experiment. In the earth's gravity field, T_c was located by observing the fluid's decomposition from one-phase into two-phases. However, in microgravity, where the critical fluid is not stratified, direct observation of the fluid close to T_c is troubled by the phenomenon of critical opalescence. Moreover, in microgravity it is difficult to distinguish between the large density fluctuations just above T_c and the occurrence of real bubbles and drops just below T_c. Fortunately, light scattering near CP offers a convenient tool to locate T_c. Phenomenologically, light scattering near CP may be explained by the phenomenon of critical opalescence: the closer to CP, the higher the intensity of the scattered light [1,7,8].

Whereas on earth the influence of the gravitational density gradient severely complicates the application of this method (see section 2.4.1), in microgravity its advantage is obvious since the fluid's density remains critical throughout the fluid when T_c is approached. Therefore, during the experiment, the critical temperature was re-determined by analysis of the WALS signals during the slow cooling ramp of the test cell through T_c. It was found by the location of the peaks in the scattering intensity in the WALS channels that the T_c of the sample was 25 mK below that determined on earth (on the scale of the sensor). In fig. 6.1, the scattering intensity is displayed for three different WALS channels while crossing the newly identified T_c.

Figure 6.1 WALS at 22°, 30° and 38° during crossing of T_c. Each curve is labelled by its corresponding fibre.

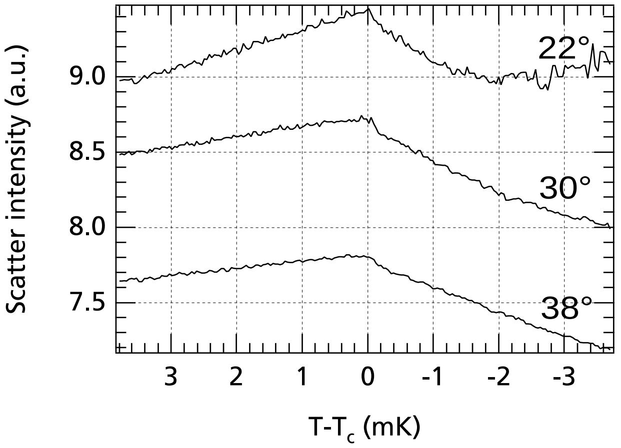

[†] Note that the total power to the system is divided between fluid and substrate.

By observing the fluid through direct visualization periodically during this cooling ramp, though obscured by the above mentioned effects, the crossing of T_c was confirmed by phase separation. In fig. 6.2 the direct visualization of the fluid at 10 mK below T_c is displayed. Due to the shape of the scattering chamber the field of view is a rectangle of 5×8 mm. The bright spot in the centre due to the narrow laser beam is just visible. The sample contents was checked again on earth several months after the mission by the position of the meniscus in crossing T_c. We found that there is no measurable leakage and we conclude that the difference is a consequence of thermistor drift. As the thermistor drift is negligible during the individual measurement runs, this drift is of no consequence for the experiments.

Figure 6.2 Coexisting phases at 10 mK below T_c in μg visualized.

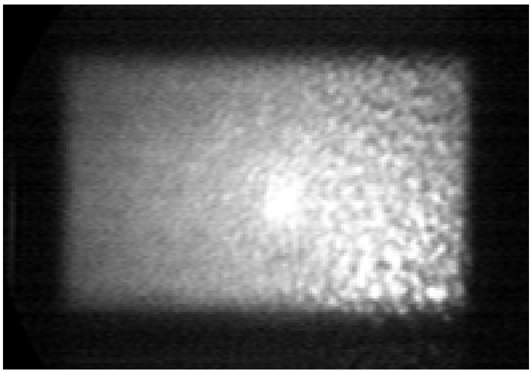

6.1.3 Heat flows

In fig. 6.3 the expected heat flows following heating by the gold plate are displayed schematicly. The double line arrows refer to the initial division of the generated heat between the fluid and the substrate, causing the appearance of a diffusion layer in the fluid adjacent to the heater. Part of the heat that enters the fluid by diffusion is transferred immediately by the PE causing a homogeneous rise in the temperature in the entire sample. The thus created temperature difference between the fluid and its surroundings will introduce additional heat flows which are represented in this figure by the single line arrows.

Figure 6.3 Schematic display of heat flows during heating with the plate heater.

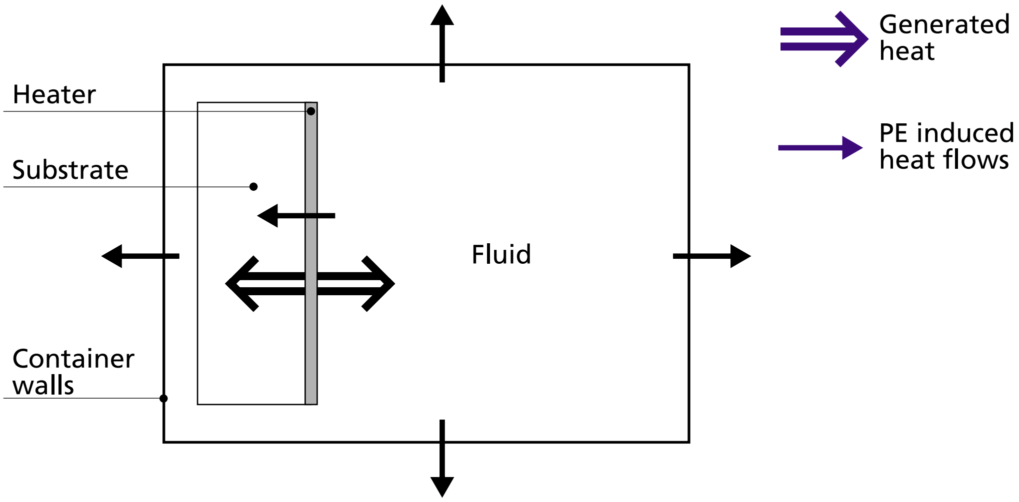

In the space experiment, altogether 66 heating runs were performed. During and following a heating run, two mechanisms of temperature change were certainly apparent. From the IF profiles we clearly see a diffusive thermal boundary layer (bent fringes and/or a growing 'shadow') and from detailed analysis we determine a rapid spatially-uniform fringe shift which must be interpreted as a homogeneous density change in the bulk of the fluid. The latter information is obtained across the parts of the interferograms representing the bulk (far away from the developing boundary layer). An example is shown in fig. 6.4. It is notable that density variations in the bulk can not be observed by 'the naked eye' because changes are less than 1% of the original fringe pattern. Moreover, our analysis confirms that the PE does not alter any existing density gradients in the sample but acts uniformly across the fluid (see for instance fig. 2.2), as also indicated by Guenoun et al. [82].

Figure 6.4 Interferometry fringes (a) before heating (t=0 s), and (b) at time t=57 s after the onset of heating.

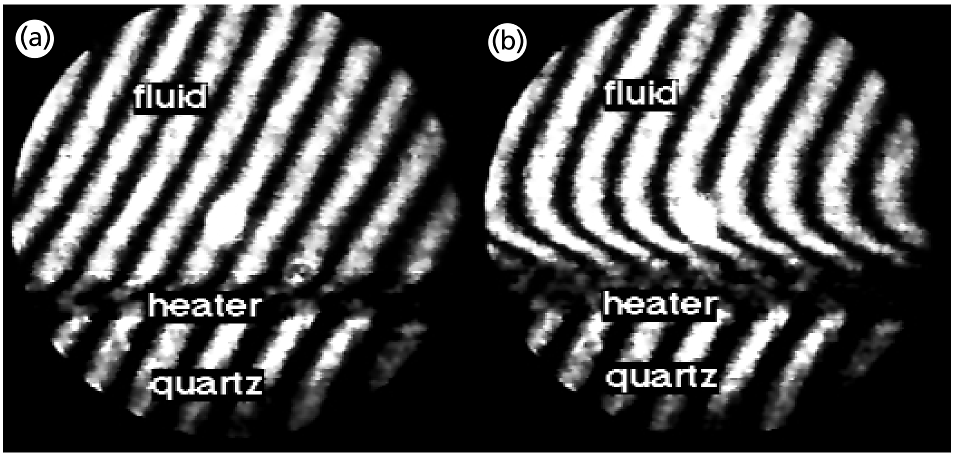

The mechanisms of heat transfer were explored experimentally in a wide dynamic range. After the mission, by detailed analysis, the useful dynamic range was established critically. As a result, data from some heating runs were discarded in the quantitative investigation, based upon three different arguments. Firstly, already during the experiment, we realized by the real-time analysis in the DUC that in some occasions the fluid had not reached a 'quasi steady state'. Only after the mission we discovered that in some of these occasions indeed the inhomogeneities proved to be too big to handle. Secondly, analysis also showed that in some occasions a current was applied that was too low for an accurate determination of either the PE by the temperature measurements of the bulk, or the D_T by the density measurements through interferometry. Thirdly, the analysis of the interferograms at temperatures closer to T_c than 5 mK turned out to be troubled too much by the critical opalescence to extract any worthy results from it.

6.2 Data analysis

As far as heat transfer is concerned, two sorts of data were provided for analysis, i.e. temperature data and interferograms. Temperature sensors are present in the fluid, the heater substrate and the cell boundaries. The fluid sensor measured the temperature of the bulk, the substrate sensor was intended for determination of the division of the pulse heat and the sensors in the cell boundaries enabled the monitoring of thermal equilibrium. Interferograms cover the boundary layer, from which D_T is determined, and a significant part of the bulk for bulk density change measurements.

6.2.1 Temperature and density

The readings of the various thermistors were acquired by CPF each second. The temperature indication was in the form of a difference from the set temperature of the thermostat, T_{set}, i.e. the temperature at which the transient heating runs were performed, which, in turn, is defined in terms of the difference to T_c. Since, moreover, it was possible to “null” the thermistors at any time, their readings could be obtained at a maximum resolution.

The capability of the fluid thermistor to trace accurately the fast, isentropic temperature changes in the bulk, as we approach the critical point, is a matter of serious concern. To investigate this issue, simple calculations of the thermistor response have been made (appendix D) from which a conclusion arises that the thermistor response gets better and better as T_c is approached! The physical reason for the good response near to T_c is that the heat flow through the boundary layer around the thermistor gets larger as the thermal conductivity of the fluid increases.

The sensitivity of the temperature measurements was $\Delta T/T \approx 10^{-8}$, which allowed the determination of the bulk temperature changes associated with the gold layer heating pulses. In our set up, the sensitivity of the density measurements was $\Delta\rho/\rho \approx 10^{-5}$, which, however, did not permit the accurate determination of the corresponding small bulk density changes. The larger density changes of the bulk resulting from changes in T_{set} could be measured easily.

6.2.2 Heating pulses

In order to accomplish the transient heating of the fluid at constant power, constant-current heating pulses were applied to the fluid by the plate heater. As pointed out in section 2.2.3, the total power dissipated by the plate heater, P, does not go entirely to the fluid but part of it (q_s) is absorbed by the quartz substrate. This energy decomposition is dictated by the thermodynamic and transport properties of the fluid and the quartz (appendix A). Knowledge of the precise amount of energy that enters the fluid is of paramount importance for the solution of eq. (2.34). An obvious relation for the power q_f that goes into the fluid is:

$$q_f = \frac{P}{1 + q_s/q_f} \;. \tag{6.1}$$

In order to calculate the dissipation ratio q_s/q_f, here it is assumed that heat travels inside both the quartz and the fluid according to the well known Fourier equation with a constant power source at the interface. In appendix A it is shown that the dissipation ratio is equal to the inverse impedance ratio of the fluid and the heater substrate, σ_h. Note that the PE temperature rise in the fluid close to the heater is included in the heat-loss term as the heater surface also is regarded as a heat-loss wall, thereby leaving q_f time independent (see section 2.2.3).

Figure 6.5 shows a plot of the fraction of the total energy that enters the quartz, $\tilde{q}_s \equiv q_s/P$, at different distances to T_c. The solid line represents predictions arising from the calculated dissipation ratio where fluid properties are taken from the equation of state (EOS) by Abbaci and Sengers [81] and diffusivity values are used from the measurements by Jany and Straub [36]; the data points are derived from fits to temperature versus time profiles measured by the thermistor in the quartz plate. It shows that less and less energy goes to the substrate as T_c is approached, thanks to the decreasing thermal impedance of the fluid (see appendix A).

Figure 6.5 Fraction of total delivered energy that enters the heater substrate.

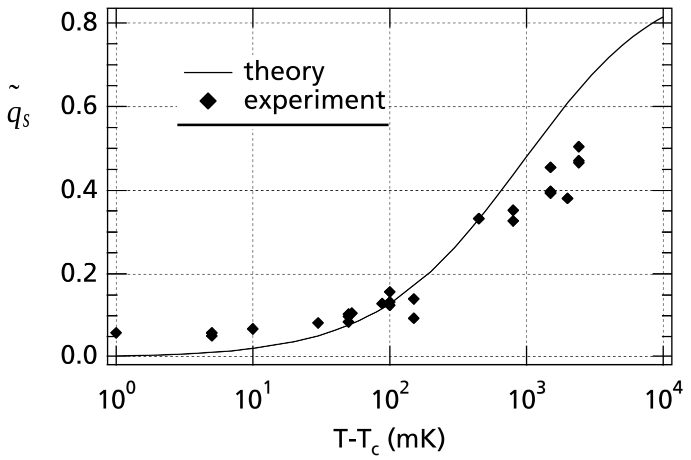

The discrepancy between measurements and predictions may be attributed to several possible sources of error in the derivation of $\tilde{q}_s$ from the measurements. In the calculation of the temperature profiles to which the measurements are fit, the assumption is that of two half infinite bodies with a heater at their interface. Whereas the error that is introduced by this assumption is negligible for the actual dissipation ratio at the heater, for the temperature change at the location of the thermistor in the substrate this is not the case. Actually, one expects to measure a lower increase in temperature than predicted at this location, due to inevitable losses to the substrate surroundings. Indeed, far from T_c the measurements show this tendency. Approaching T_c another effect becomes increasingly important to the temperature rise at the location of the thermistor. When most of the dissipated energy goes to the fluid, the temperature increase due to the PE of the fluid around the substrate and the thermistor wires becomes significant in comparison to the heat coming directly from the heater. Therefore, close to T_c one expects to measure a higher increase in temperature than predicted. Taking also into account the reduced sensitivity of the thermistor in the substrate (see section 3.3.2), the comparison between measurements and predictions is considered satisfactory.

Far from CP the thermal properties of SF_6 are well known from g=1 literature data, while in the approach to CP the increasing uncertainty in these properties is of decreasing importance to the calculation of the dissipation ratio. For the reasons outlined above we consider the measurements of the dissipation ratio less accurate than the calculated one and henceforth, the literature values [36,81] have been used to calculate the temperature dependent fluid-quartz impedance ratio. This ratio further is used in eq. (6.1) for solving the heat transfer equations on the fluid's side.

6.2.3 Apparent wall properties

In order to implement eqs. (2.34), (2.36) and (2.37) for comparisons with the data of the isentropic temperature rise in the bulk, the transport properties and the surface area of all the cell walls need to be determined. This is not an easy task because of the complex geometry of the cell and the several different materials utilized in its construction. Among the various materials of construction we have identified the five most significant in view of their relative contribution to heat losses. These five materials exhibit the highest inverse thermal impedance values together with appreciable surface areas for heat exchange. Table 6.1 lists these parts and their corresponding inverse impedance and surface area values. The inverse thermal impedance values are provided by the manufacturers while the surface areas are evaluated by simple geometrical considerations.

However, calculating the surface areas - available for heat exchange - in a configuration of such complexity is expected to give only very conservative values since the possibility cannot be excluded that minor geometrical imperfections can have a large effect. Indeed, preliminary calculations taking into account the individual wall materials gave an unsatisfactory correlation between predicted and measured isentropic temperature changes. Therefore, as customarily adopted in the literature, it seems appropriate to include all effects in just one single set of phenomenological parameters which will be referred henceforth as the apparent inverse thermal impedance, $\lambda_a / \sqrt{D_a}$, and the apparent surface area, S_a, of the container walls. Values for these parameters may be obtained from a "best fit" procedure of eq. (2.34) to experimental data. The values produced in this way are also included in table 6.1. As shown, the apparent inverse thermal impedance is, as expected, in the order of magnitude of the specified impedances but the apparent surface area indeed turns out to be larger than estimated.

Table 6.1 Inverse thermal impedance and surface area of wall materials.

Wall material	Inverse thermal impedance $\lambda_i / \sqrt{D_i}$ (Ws$^{1/2}$/m^{2}K)	Surface area S_i (mm^2)
Aluminium	2.4 10^4	240
Synthetic quartz	6 10^2	540
Fused silicon	6 10^2	690
Kel-F	5 10^2	470
Invar (NILO-36)	8 10^3	100
Apparent properties	6 10^3	2.5 10^3

6.3 Piston Effect

In order to determine the thermal conductivity or diffusivity to within say 1 mK from the critical point, a microgravity environment is of special value because it provides a means to eliminate density stratification and convection. From the early stages of this work it was realized however [21-24], that under these conditions another process of temperature change in a fluid (referred to as the adiabatic effect (AE) or piston effect (PE)) becomes of increasing significance during any transient heating as CP is approached. Fundamentally, this PE is not a mechanism of true heat transport (contrary to the statements made in some of the literature) but it is an energy transfer effect. It is a bulk response to local heating resulting from isentropic compression in a finite sample. Heating at the boundary of such a sample causes thermal expansion of the adjacent fluid layer and, consequently, a pressure increase everywhere in the fluid. This pressure increase results in an essentially isentropic increase in temperature and density uniform throughout the fluid. Various experiments confirming the uniform rapid thermal response in a near-critical fluid have been reported by Boukari et al. [25], who used ground-based equipment, and by Klein et al. [26], Bonetti et al. [27], Straub et al. [28] and Michels et al. [29] working on microgravity platforms.

The interpretation of the PE in a practical system is complicated by the fact that it introduces an additional heat flow through the walls surrounding the fluid. During the rapid uniform temperature increase these walls remain colder than the fluid itself and a boundary layer develops at these walls: energy will flow out of the fluid, cooling it again by adiabatic expansion. Ferrell and Hao [55] were the first to study analytically the PE including this secondary effect, following a model in which the fluid is initially at a uniform temperature that is different from that of the container. They concluded that this secondary effect depends on the ratio between thermal properties of the wall material and those of the fluid; since the latter exhibit singular behaviour near the critical point, the fraction of heating power dissipated through thermal conduction, in terms of distance to the critical point, will depend strongly on actual thermal parameters of the walls. Beysens et al. [83] experimentally confirmed this effect qualitatively. However, to account for it in a quantitative way one has to calculate the overall cell wall parameters which, for most actual cell configurations cannot be accomplished with reasonable accuracy.

However, such a quantitative description of the PE is necessary if measurements of the transient temperature increase in a fluid near the critical point are to be used to study the thermal conductivity or diffusivity in the near-critical region. This is because the contribution of the PE generally must be eliminated from the measurements of temperature rise before they are interpreted in terms of a simple conduction equation.

Part of this thesis concerns a quantitative description of the PE in measurements in a sample of near-critical SF_6 under microgravity conditions, following a heating with constant power at a flat boundary surface in a range down to $T - T_c = 1$ mK. This should enable a separation of the PE from true heat transport effects in data of measurements on the thermal conductivity or diffusivity in the near-critical region of pure fluids. The results described in the next section show consistently the role of the PE in a pure critical fluid surrounded by finitely conducting boundaries [84].

6.3.1 Results and discussion

It has become clear that the thermal properties of the wall material play a significant role in the actual quantitative temperature change of the PE. Attention is directed to the comparison between the values of the fluid's inverse thermal impedance with the values of the same property of the wall materials. Figure 6.6 displays the inverse thermal impedance values against the distance to T_c. It can be seen clearly that for $T - T_c < \sim 200$ mK the fluid's inverse thermal impedance attains a value higher than the apparent inverse thermal impedance of the walls, while for $T - T_c < \sim 40$ mK the fluid even becomes more conductive than any wall material. The notion that the finite thermal impedance of the walls governs the energy losses to the surroundings then implies that near $T - T_c = 200$ mK a *conduction crossover* takes place as regards the thermalization time of the sample. This is better demonstrated in fig. 6.7 where the characteristic time t_c (eq. (2.29)) is plotted with respect to distance to T_c. It is seen that far away from the critical temperature, t_c appears to decrease rapidly as T_c is approached. Getting closer to T_c it starts to level off gradually and finally a weak rise is observed proportional to c_V^2 (see section 2.2.2 on page 14), revealing clearly the crossover to a new equilibration regime. For the fitcurve presented in fig. 6.7 the best fit values through our data have been employed for the apparent inverse thermal impedance and surface area (see section 6.2.3).

Figure 6.6 Comparison between the inverse thermal impedance of the fluid and the wall materials.

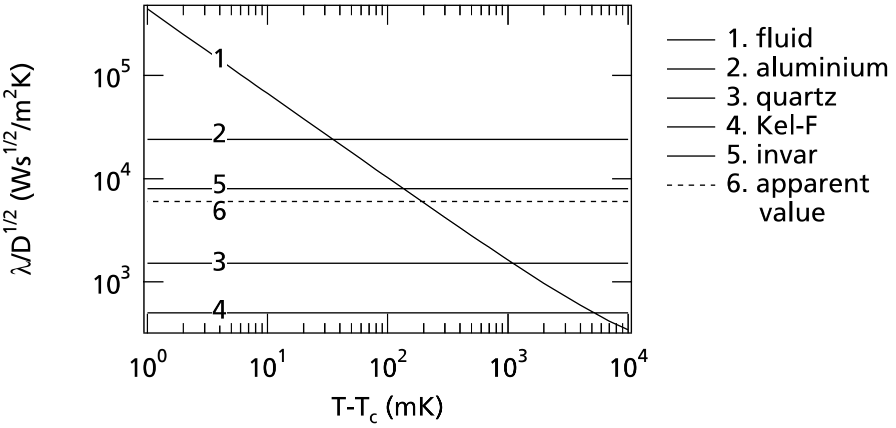

Figure 6.7 Variation of the characteristic time, t_c, with the distance to T_c.

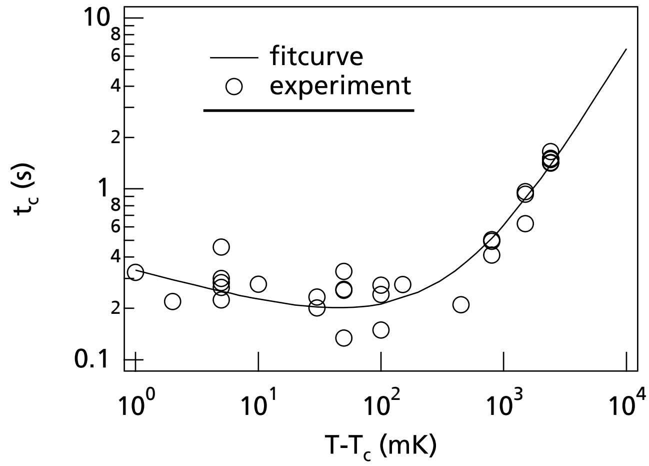

Figure 6.8 Theoretical predictions of isentropic temperature rise in our sample fluid accounting for heat losses to the heater substrate and through the other surrounding walls.

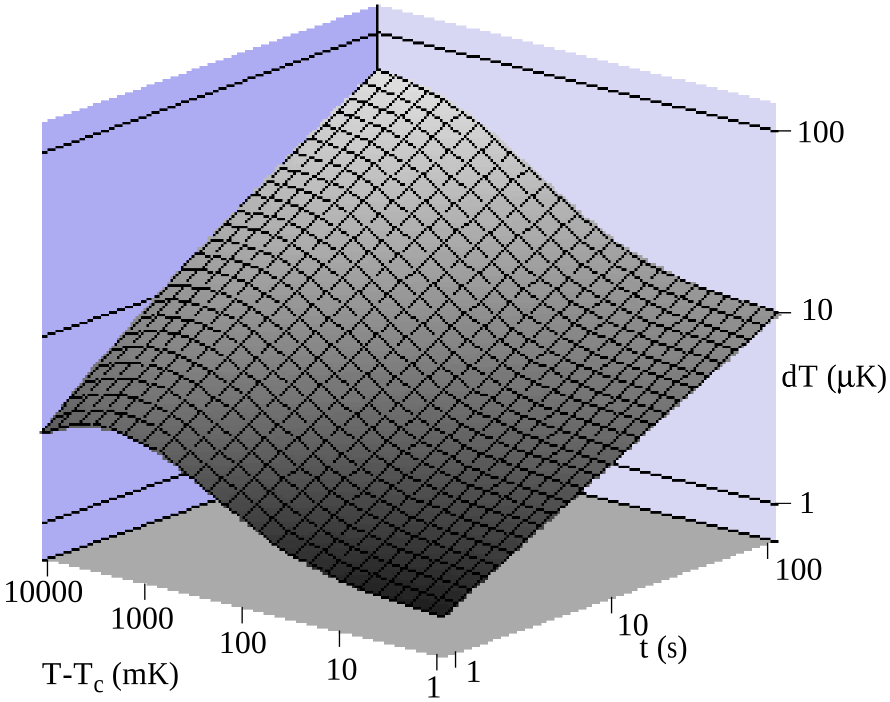

The influence of the finite thermal impedance of the walls to the thermal response of our sample during heating at the boundary, is illustrated in fig. 6.8. This is a 3D plot of the predicted isentropic temperature increase in the bulk (eq. (2.34)) versus heating time and distance to the critical point. For clarity, predictions for only one value of dissipated power are presented. Fit values of the apparent thermal impedance and surface area (see section 6.2.3) have been employed in the calculations. Upon inspection of the graph, the square-root time dependence [eq. (2.37)] of the temperature increase is recognized. At a specific time after the onset of heating, this graph also shows that, as T_c is approached, there is a characteristic levelling off of the temperature increase. In view of the anomalous behaviour of the thermodynamic properties in this region, this may seem surprising. However, this can be understood when one realizes that far from CP the strongly divergent thermal impedance of the fluid governs the behaviour, whereas close to CP the weakly divergent c_v is the leading property. A little further from T_c the theoretical curves exhibit a prominent peak which becomes higher and broader further in time. This peak originates from the competition between a decreasing q_f [eq. (6.1)] and an increasing t_c as τ increases (for $\tau > 10^{-3}$).

Figure 6.9 Thermistor readings relatively far from CP during heat pulses of constant power and predictions by eqs. (2.34), (2.36) and (2.37).

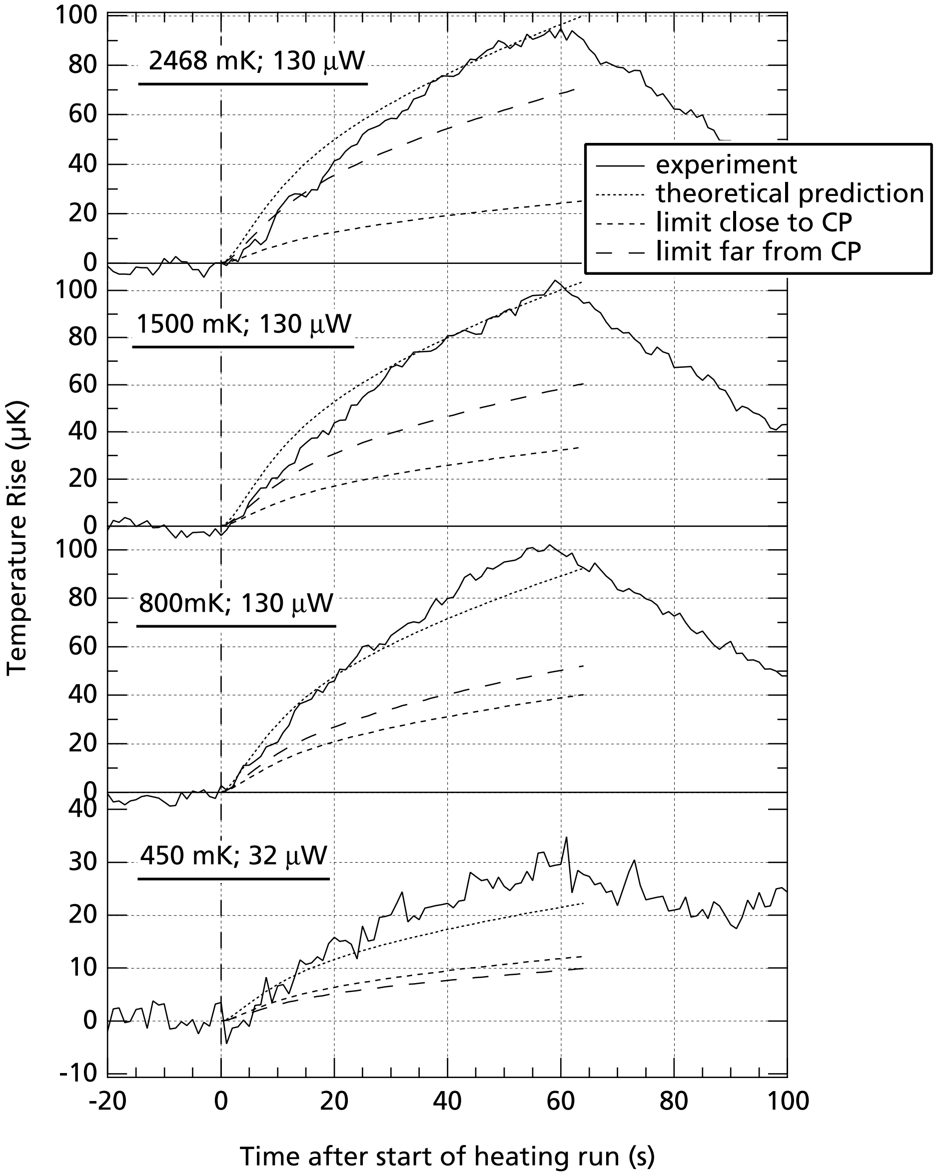

Typical readings from the thermistor located in the fluid are shown in fig. 6.9 and fig. 6.10 for eight heating runs together with the predictions according to eq. (2.34) and the limiting cases of eqs. (2.36) and (2.37). We see that our thermistor responses are essentially synchronous with the onset of heating, an important feature of the PE which is not found when dealing with thermal conduction alone. Comparison with the predictions signifies the validity of eq. (2.34). The limiting cases can be regarded as two complementary contributions to the observed behaviour [eq.(2.34)], in which the size of each contribution depends on the distance to T_c. These figures also demonstrate that for temperatures closer to T_c than 100 mK the limiting case of eq. (2.37) is applicable. Again, this complies with the notion that the fluid's thermal impedance drops below that of the apparent value of the surroundings shortly above T_c+100 mK. Apparently, at T_c+2.5 K τ is still not large enough for the other limiting case [eq. (2.36)] to hold. Necessarily, the intermediate states shown in these two figures do not permit the use of either of the limiting equations as their contributions are comparable.

Figure 6.10 Thermistor readings relatively close to CP during heat pulses of constant power and predictions by eqs. (2.34), (2.36) and (2.37).

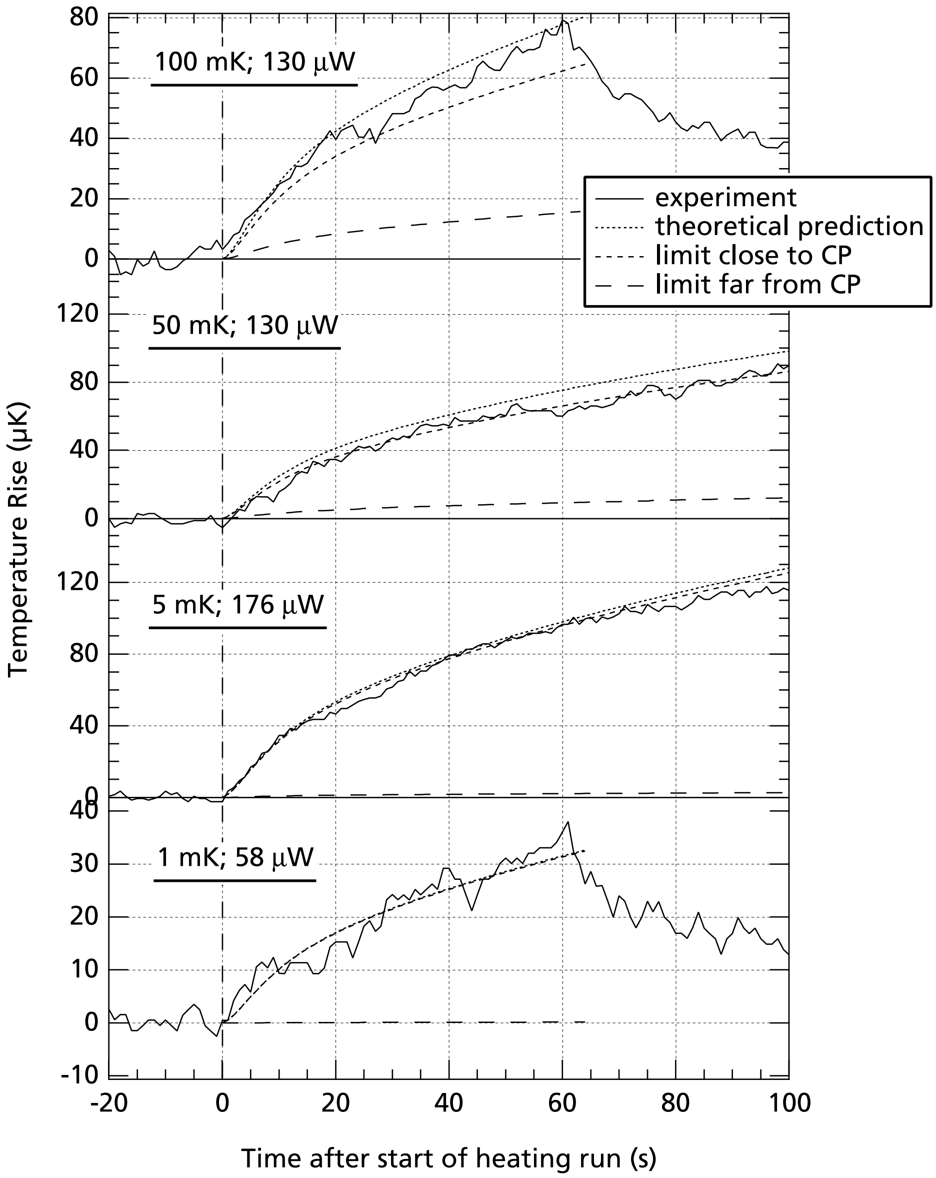

A comprehensive set of measurements is presented in fig. 6.11 where the observed isentropic temperature rise in the bulk is plotted against $T - T_c$ at different times after the onset of heating. The data are normalized with respect to the total dissipated power P entering the fluid [eq. (6.1)] in order to facilitate the presentation. Solid lines are best fits through the data. In concurrence to the main features outlined theoretically in connection with fig. 6.8, fig. 6.11 shows nicely the characteristic levelling off of the temperature increase close to T_c as well as the idea of a peak further away from T_c. Unfortunately, we have not measured far enough from T_c to witness also accurately the temporal behaviour of the peak in the temperature rise. A closer look at fig. 6.11 reveals that at small times the temperature increase falls behind the theoretical one. This is because in the theoretical curves the experimental response time of the temperature reproduction (a combination of both the response times of the thermistor and the CPF, amounting to approximately 3-4 seconds) is not incorporated. The experimental data, of course, exhibit this response time. In the 'theoretical' predictions of figs. 6.9 and 6.10, it has been accounted for.

Figure 6.11 Experimental data of isentropic temperature rise per Watt of dissipated power at several times during heating runs versus the distance to T_c.

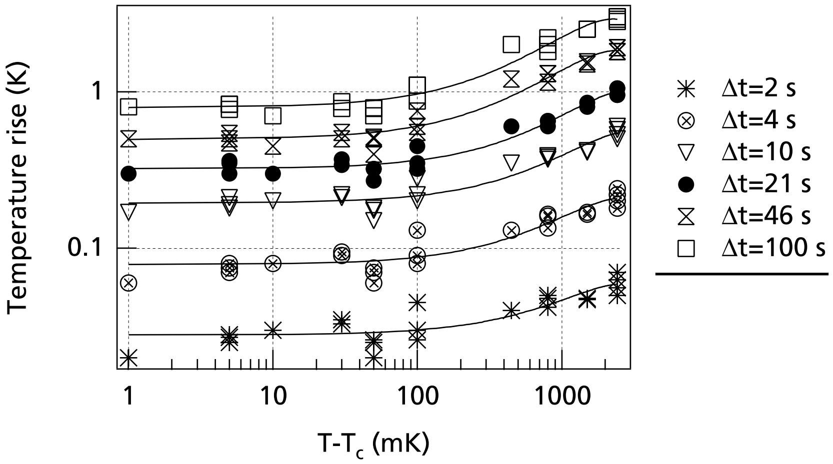

Figure 6.12 shows the measured amplitude A as well as the predicted A (see eq. (2.35)) versus the distance to the critical point. Again, the experimental data is in good agreement with the predictions manifesting the significance of the role of the properties of the surrounding walls to the thermalization of a critical fluid.

Figure 6.12 Comparison between predictions and experiment as regards the amplitude A.

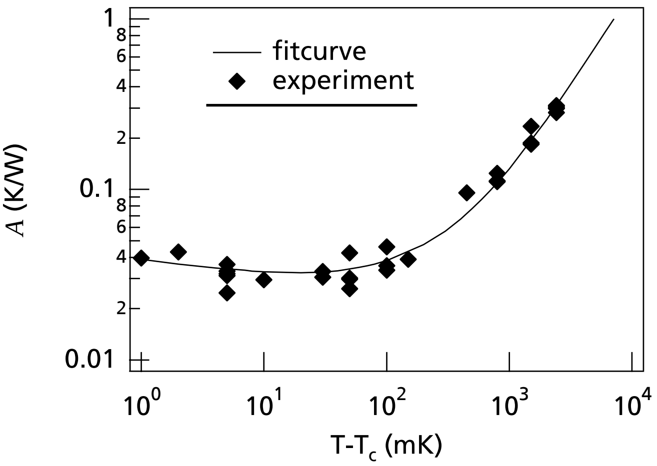

6.3.2 Conclusions

The present study provides new theoretical and experimental information regarding the mechanisms of heat transfer in a near-critical fluid. Two dominant mechanisms have been identified: a diffusing thermal boundary layer adjacent to heated surfaces and a homogeneous isentropic temperature change across the entire volume of the sample. The present study was motivated by the paucity of information in the literature regarding the behaviour of the PE in a real experiment of transient heating of a near-critical fluid with bounding walls of finite thermal impedance.

The isentropic temperature rise that follows transient heating of a near-critical fluid has now been determined in a microgravity environment and is described remarkably well by a further development of the theoretical model proposed by Ferrell and Hao [55]. The important feature of this description is that the equilibration process is profoundly influenced by the thermal properties of the solid surfaces bounding the fluid even though the isentropic heating effect itself is uniform throughout the bulk of the fluid and is independent of existing gradients. This influence is clearly illustrated by fig. 6.7 where the crossover to a new equilibration regime is observed as T_c is approached.

The thermal behaviour of the container can be characterized in the description by means of a single set of phenomenological parameters enabling even in a container of complex geometry the separation of the PE from true heat transport effects in a quantitative way. This conclusion will permit subsequent analysis of the longer-term transient behaviour to determine the thermal conductivity and diffusivity of the fluid near to the critical point.

6.4 Thermal diffusivity

The processes of heat transfer are studied in a controlled way. A measuring technique is used, similar to that introduced by Becker and Grigull [37-40], in which the propagation of a plane thermal stepwise disturbance into an otherwise homogeneous sample is observed by interferometry. Due to the divergence of the isobaric thermal expansion coefficient this method becomes increasingly sensitive closer to the critical point, so that a very small heat input is required, allowing the introduction of thermal gradients covering a wide range of values. Analysis of the density profiles have resulted in experimental values for the thermal diffusivity in a range down to 5 mK from T_c.

6.4.1 Methods for the determination of the thermal diffusivity

Originally, it was intended to determine spatial density profiles at several times upon heating with the gold layer, out of which D_T can be found accurately by fitting to (ρ ,x,t)-data sets. Unfortunately, as discussed in section 4.3, we were forced to turn to an alternative procedure which is based on the development of the shadow that arises in the interferograms adjacent to the image of the heater. In “Shadow evaluation” on page 48, the position of the shadow front in time upon heating with a constant heat flux is calculated in the PA. Out of the calculations we may conclude that, in the PA, the shadow development can be characterized by two types. At the onset of heating the shadow starts to grow, gradually levelling off to a maximum which is reached at a time t_m, referred to as type II. From that time on the shadow remains at its maximum size $M Z_0$, referred to as type I. Both types can be described by the same two parameters t_m and Z_0. The general behaviour of the shadow front z_f' in the PA is sketched in fig. 6.13, in which the two types, t_m and $M Z_0$ are indicated.

Consequently, from the shadow front development, it may seem straightforward to find both Z_0 and t_m enabling the subsequent determination of D_T out of the definition for t_m (eq. (4.28)). For instance, the value of Z_0 is derived easily from the plateau value of z_f' (type I) and the value of t_m can be found by determining the time at which the behaviour changes from type II to type I. Obviously, the accuracy in the determination of D_T by this method hinges on the accuracy in the determination of both Z_0 and t_m. Where Z_0 might be determined accurately by averaging the plateau value over a substantial time (although time is limited in a space experiment), the accurate determination of t_m is much harder to attain. Principally, the accuracy is limited by the time-resolution of the IF images. During IML2, the images were displayed generally only at 1/6 Hz although in some events the images were displayed at 30 Hz. For small values of t_m this posed serious problems for its determination. But on top of that, in the last part of type II, by nature, z_f' levels off to its plateau value in a smooth manner, appearing to have reached already type I. For this reason, it was very difficult to distinguish between the two types near $t = t_m$. The combination of the above mentioned complications reduces considerably the accuracy in the determination of t_m by this method, typically to approximately 10%.

Figure 6.13 Shadow front movement in the PA.

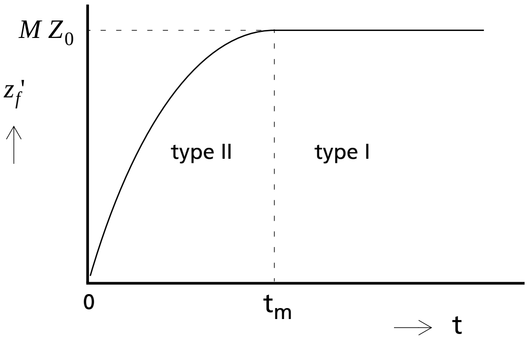

Another difficulty that arises in the application of the method described above is in the approach to CP. Looking at the critical dependence of both Z_0 and t_m, we see that both diverge approaching CP:

$$Z_0 \sim \frac{\alpha_p}{\lambda} \sim \tau^{-0.67} \tag{6.2}$$

$$t_m \sim \frac{Z_0^2}{D_T} \sim \tau^{-2.01}\,. \tag{6.3}$$

Necessarily, in order to capture in a IF image type I behaviour, on approaching CP a compressed image and considerable heating time is needed. In the present optical configuration of CPF it turned out that, in our time-limited space experiment, the captured behaviour of z_f' was totally type II for temperatures closer than 1000 mK to T_c (at $T - T_c = 500$ mK $t_m \approx 1$ hr for a power density of 0.5 W/m^2 and the optical layout for the CCD camera). Moreover, in those cases where type I behaviour was detected, the light paths did not concur to the PA (see section E.1) causing a severe complication. Hence, although at first sight the abovementioned method looks promising, in practise it is unfeasible.

A practical method to derive D_T out of the shadow front development is to fit eq. (4.26) to z_f' when its behaviour is still type II. This fit comprises the two parameters Z_0 and t_m. Moreover, although Z_0 depends on many quantities, of these we consider the only real unknown quantity to be D_T. We may rewrite eq. (4.29), which defines Z_0, into:

$$Z_0 = \frac{1}{K_2}\frac{q_f}{S_h}\frac{1}{D_T}\frac{\alpha_p}{c_p}\,. \tag{6.4}$$

Using the thermodynamic relations (2.7) and (2.8), eq. (6.4) can be expressed as:

$$Z_0 = \frac{1}{K_2}\frac{q_f}{S_h}\frac{1}{D_T}\frac{\rho}{T}\left(\frac{\partial T}{\partial p}\right)_\rho\left(1-\frac{c_v}{c_p}\right) . \tag{6.5}$$

Apart from D_T and the ratio of the specific heats, the thermodynamic quantities in this expression behave smoothly near CP and therefore these values are well known from the $g = 1$ literature. Furthermore, on approaching CP the ratio of the specific heats can be neglected rapidly, while in the region where this ratio may not be neglected, theoretical values can be used safely as the resulting uncertainty in the ratio contributes only little in the value of Z_0. For these reasons we consider D_T as the single unknown thermodynamic quantity in the expression for Z_0. The power density to the fluid, q_f/S_h (see section 6.2.2), is known to a satisfactory level. Relatively far away from T_c the transport properties concerned (λ and D_T) are known, while in the approach to CP the increasing uncertainty in these properties is of decreasing importance to the calculation of the power density to the fluid. The 'optical' quantity K_2 (eq. (4.25)) we consider to be known (see chapter 5). Since t_m depends only on Z_0 and D_T, we allow a fit of eq. (4.26) to the development of the shadow front to be reduced to one parameter, i.e. D_T. The one parameter fit (O.P.F.) was used in those cases where the PA was applicable. This fit was provided by a data analysing program called Igor Pro by WaveMetrics, Inc.. In those cases where the PA was not applicable we used numerical inversion (N.I.) to determine D_T.

6.4.2 Results and discussion

Of the 66 heating runs carried out in the space shuttle finally only 28 were found to be within useful dynamic range (see section 6.1.3) for analysis. Only at temperatures closer to T_c than 200 mK the PA was applicable, in which case the O.P.F. could be used. The results of the thermal diffusivity measurements along the critical isochore are summarized in table 6.2. This table consists of the applied determination method, the temperature difference with T_c at which the measurements are performed, the current that was utilized to accomplish the heating and the resulting D_T including its accuracy. The accuracies resulting from the O.P.F. are standard deviations which are produced by the fitting program. The accuracies resulting from the N.I. are estimated with an “eyeball” fitting procedure. Our data can be approximated adequately in terms of a power law relation by the formula

$$D_T = (1.77 \pm 0.03) \cdot 10^{-9}(T - T_c)^{0.868 \pm 0.006}\ \mathrm{m^2/s} \tag{6.6}$$

over the full measured temperature range.

Table 6.2 Measured thermal diffusivities.

nr.	method	$T - T_c$ (mK)	current (mA)	D_T (10^{-10} m^2 s^{-1})
1	N.I.	2468	6	38±3
2	N.I.	2468	6	40±5
3	N.I.	2468	6	42±3
4	N.I.	2468	6	41±4
5	N.I.	2468	4	39±4
6	N.I.	2000	3	31±3
7	N.I.	1500	6	25±4
8	N.I.	1500	6	26±4

Table 6.2 Measured thermal diffusivities.

nr.	method	$T - T_c$ (mK)	current (mA)	D_T (10^{-10} m^2 s^{-1})
9	N.I.	1500	3	27±3
10	N.I.	1025	3	17±1
11	N.I.	800	6	15±2
12	N.I.	800	6	13±2
13	N.I.	800	6	14±2
14	N.I.	450	3	9±1
15	N.I.	325	1.5	6.6±0.2
16	O.P.F	150	3	3.32±0.10
17	O.P.F	106	3	2.27±0.08
18	O.P.F	100	6	2.43±0.08
19	O.P.F	100	4	2.62±0.08
20	O.P.F	50	6	1.25±0.04
21	O.P.F	50	2	1.24±0.05
22	O.P.F	50	2	1.28±0.07
23	O.P.F	45	1	1.13±0.08
24	O.P.F	30	4	0.87±0.02
25	O.P.F.	30	3	1.01±0.07
26	O.P.F	10	5	0.35±0.03
27	O.P.F	5	7	0.18±0.01
28	O.P.F	5	3.5	0.17±0.01

Generally, the shadow front developments are fit well by the expected behaviour, either in the PA (eq.(4.26)) or as calculated numerically. Examples close to T_c, where the PA is valid, are shown in fig. 6.14 together with the one parameter fits. Since the sizes of the shadows at low currents usually are smaller, the accuracies are less accordingly. In fig. 6.15, examples are shown from heating runs for which the PA is not applicable. Also shown in this figure are numerical predictions to which the shadow front development is compared. In some of these occasions the behaviour was not very sensitive to D_T, leading to lower accuracies correspondingly.

Figure 6.14 The shadow front close to T_c.

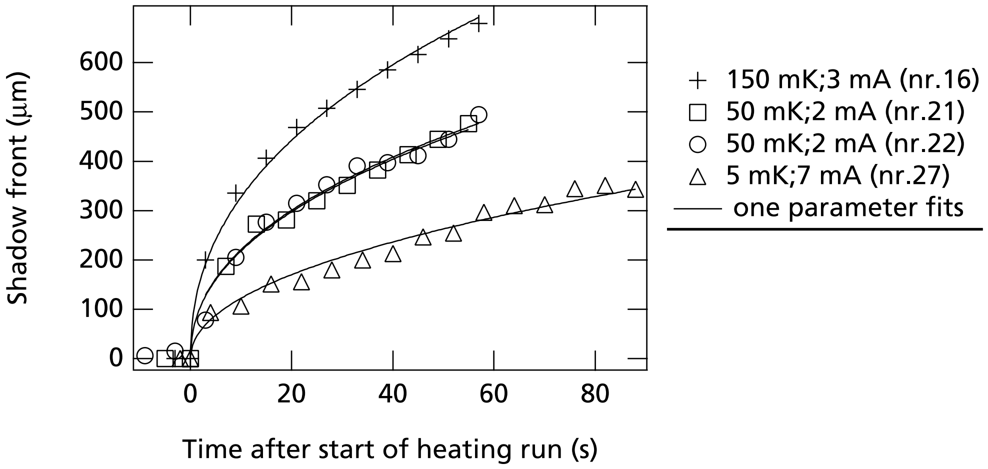

Figure 6.15 The shadow front far from T_c.

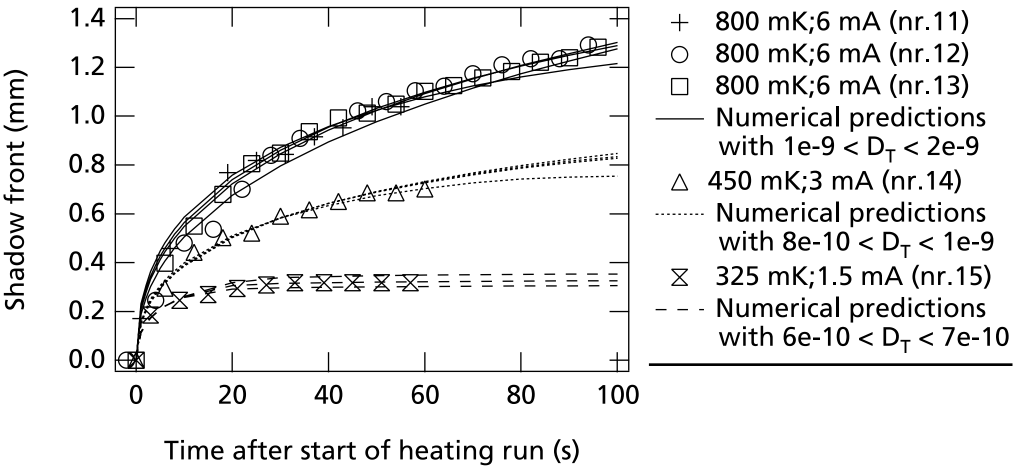

In fig. 6.16, our D_T-values are displayed versus $T - T_c$. This figure also includes earth-based results by Feke et al. [85] and Jany and Straub [36], which both deduced their values of D_T from light scattering. In this figure, the results by Feke et al. [85] are represented by a fit through their data and the results by Jany and Straub [36] are represented by a power law description as given in their paper. These two sets of data are in mutual agreement. In the temperature range where our data and the light scattering data overlaps, our data agrees fairly well with both abovementioned results. Considering the full temperature range our data give rise to a slightly larger slope in the lower panel of fig.6.16 than those of Jany and Straub [36]. The earth-based results by Letaief et al. [86] are consistent with our data down to T_c+100 mK, but closer to T_c their data exceeds significantly all data considered above. Less recent, earth-based measurements of D_T along the critical isochore have been reported by Saxman and Benedek [87] and by Braun et al. [88], both results of which are significantly lower than all data considered above.

In a microgravity environment, the only other measurements of D_T that have been reported are those by Wilkinson et al. [89], the experiment of which was performed also with the CPF on the same Space Shuttle mission as this work. They deduced D_T-values from density changes associated with the late stage of thermal equilibration. Their values of D_T including error bars are displayed also in fig. 6.16. In the temperature range where both sets of data overlap, the measurements are in mutual agreement with the exception of the two values closest to CP at T_c+5 mK, at which our results are lower. Although this discrepancy is found only in these two values directly, it is also suggested by the temperature behaviour of D_T that is implied by the full range of the measurements (eq.(6.6)). We have not yet discovered a convincing explanation for this discrepancy. A possible cause of it may come from a wrongly assumed value of T_c, the effect of which is greater closer to T_c. Whereas in the earth's gravity field the precise location of T_c by observation of phase separation may introduce a systematic error, we believe that, as concluded from fig. 6.1 in section 6.1.2, we were able to determine T_c well within 1 mK. However, it is noted that Wilkinson et al. [89], using the same procedure to locate T_c, found that the irreproducibility of T_c was greater, close to 2 mK. Still, an error corresponding to this accuracy cannot explain the discrepancy. We are inclined to argue that the inconsistency is due to the nature of the methods. We have deduced D_T-values from an early, rapid and local response of the fluid to a relatively large temperature disturbance, in contrast to the late, slow stage of thermal equilibration in which the temperature itself is seemingly in equilibrium revealing only its behaviour through the subsequent evolution of the density distribution.

Figure 6.16 The thermal diffusivity versus temperature difference to T_c. In the middle the temperature ranges studied by the various authors are indicated.

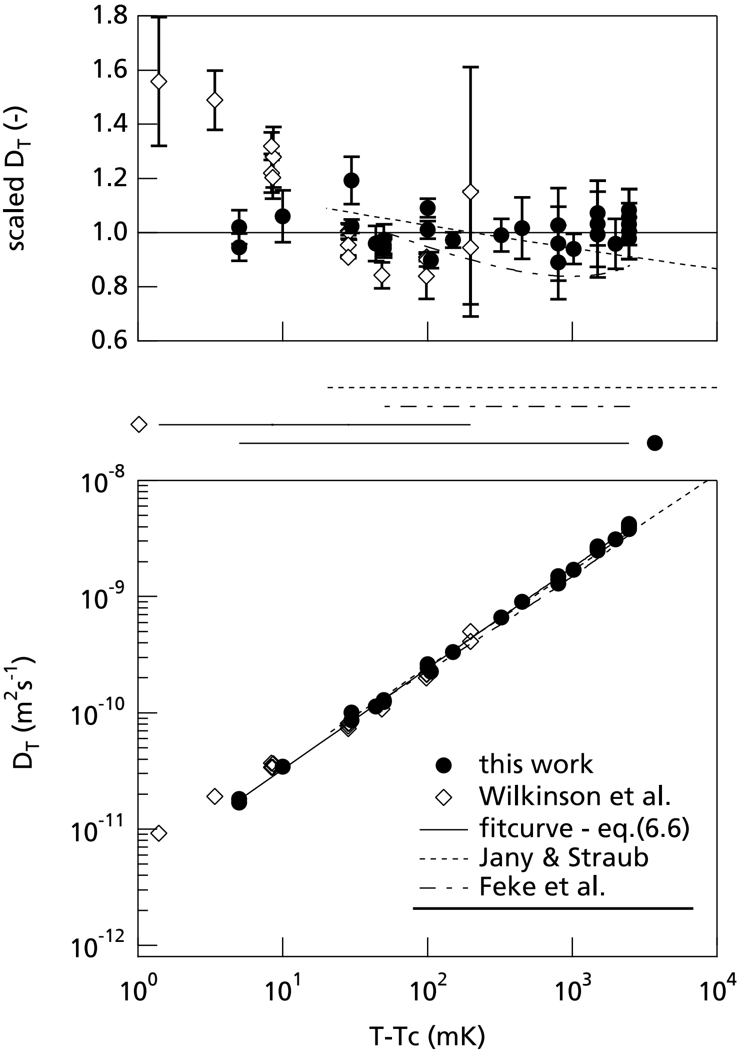

6.4.3 Conclusions

Measurements of D_T of SF_6 in a range of 5 mK < $T - T_c$ < 2.5 K are performed in a microgravity environment, closer to CP than heretofore reached in earth based experiments. The measured values of D_T are in fairly good agreement with published earth-based light scattering measurements. A discrepancy is found for values closer to T_c than 10 mK with the only other measurements published this close to CP. A convincing explanation for this discrepancy has not yet been found. A possible cause lies in the difference in the process which is observed by the two methods; we have deduced D_T-values from the early, rapid and local response to a thermal disturbance whereas in the other microgravity experiment values were inferred from slow and non-local behaviour in the late stage of thermal equilibration.

6.5 Isochoric Specific Heat

As mentioned in section 2.2.2 the Piston Effect is closely connected with the value of the isochoric specific heat c_v, which diverges weakly at the approach to CP (see eq. (2.10)). The isochoric specific heat plays an important role in the development of practical equations of state [81] and in the formulation of the behaviour of the thermal conductivity equation [90,91]. The experimental determination of this quantity in the critical region, however, has proven to be very difficult. Various methods have been employed for its measurement [92-98], all based on the determination of the change in temperature, following a calibrated heat input. The most cumbersome complication is that generally the heat capacity of the high pressure container is substantially greater than that of the sample; combined with gravity-driven convection this leads to spurious heat losses, which makes it difficult to ensure enough accuracy for the heat input figure.

Since the availability of a microgravity environment has enabled the quantitative measurement of the PE -as elaborated in this thesis- an entirely new method is proposed here [100]. This method is based on the fact that the PE essentially transfers work into heat by isentropic compression in the bulk of the sample. Therefore, simultaneous measurement of the bulk temperature and density changes enables the determination of the isentropic thermal expansion coefficient (α_s, defined in eq. (2.3)), which is directly related to c_v (see eq. (2.8)). The work, in this experiment, is generated by local heat input into the sample. The amount of heat, actually flowing into the sample fluid is less important; it only has to be sufficient to generate density and temperature changes that can be measured conveniently. This novel, intrinsically accurate method is applicable to all compressible fluids. It is especially in the critical region of definite advantage because of the fluid's anomalous behaviour, which severely complicates interpretation of measurements in the earth's gravity field (see section 2.4).

The importance of a well established microgravity environment in the application of the above-mentioned method has been evidenced in this work. Already small disturbances in the gravity level (gravity jitter) show a clear break down of the isentropic correspondence between temperature and density changes in the bulk.

Unfortunately, the possibilities of this method were recognized only during the stage of data analysis, after the mission was completed. As a consequence the data for c_v presented in this thesis were extracted from measurements done for a different purpose. Although this allows to establish the potential of this method, the actual accuracy of the measurements is far less than can be achieved in a dedicated experiment.

6.5.1 Method of analysis

In order to determine c_v from the experiment data we rewrite eq. (2.3) and (2.8) as

$$c_v = -(\rho\alpha_s)\frac{T}{\rho^2}\left(\frac{\partial p}{\partial T}\right)_\rho , \tag{6.7}$$

where

$$-\rho\alpha_s = \frac{\hat{\rho}_b(t)}{\hat{T}_b(t)} . \tag{6.8}$$

The determination of α_s therefore requires simultaneous measurement of the bulk temperature change, $\hat{T}_b(t)$, and the bulk density change, $\hat{\rho}_b(t)$.

In principle, the bulk temperature is registered at a rate of 1 Hz by the thermistor located in the fluid. When the bulk of the fluid starts heating up, the thermistor will be part of the 'cold walls', discussed in section 2.3. As a consequence, the thermistor reading will lag behind the temperature it is monitoring. This thermal lag is established easily by analysing the data. Close to CP, this might raise some concern; therefore, this matter is discussed in detail in appendix D.

As explained in section 2.3 the direct determination of $\hat{\rho}_b(t)$ is not possible, due to boundary effects. The interferogram actually records a density change $\langle\hat{\rho}(t)\rangle$, averaged over the lightpath, and eq. (6.8) should (see eq.(2.62) & (2.65)) be replaced by

$$-\rho\alpha_s = \frac{\langle\hat{\rho}(t)\rangle}{\hat{T}_b(t)}(1+E\sqrt{t})^{-1}, \tag{6.9}$$

with

$$E = \left(\frac{c_p}{c_v}-1\right)\frac{\sigma_i}{(1+\sigma_i)}\frac{2}{L}\sqrt{\frac{D_T}{\pi}}I\ . \tag{6.10}$$

By a fit of Mt^{μ} to the $\hat{T}_b(t)$-profile from the actual experiment, the value of $I = I(\mu)$ can be found (see fig. 2.5).

The fact that the fluid's container is finite constitutes a point of attention, regarding interpretation of the experimental data. Eventually, at some time $t = t_d$, one of the developing boundary layers will reach the position of measurement of either $\hat{T}_b(t)$ or $\langle\hat{\rho}(t)\rangle$. By restricting the analysis to data for which $t < t_d$, this problem can be avoided. An estimate of t_d can be made on the basis of eq.(2.39) which describes the effective diffusion layer thickness. This estimate was confirmed by analysing the data.

According to eq.(6.9), a plot of $\langle\hat{\rho}(t)\rangle$ versus $\hat{T}_b(t)$ during heating generally will show the behaviour as indicated by the solid curve in fig.6.17. The dashed straight line in this figure is the asymptotic behaviour towards the origin, i.e. for small times, the slope of which is determined by $-\rho\alpha_s$. A fit of eq.(6.9) to $\langle\hat{\rho}(t)\rangle$ versus $\hat{T}_b(t)$ may yield the values of both $-\rho\alpha_s$ and E. When E is known, $\langle\hat{\rho}(t)\rangle$ can be plotted versus $\hat{T}_b(t)(1+E\sqrt{t})$ yielding a straight line equal to the asymptotic behaviour. Since we presume knowledge of E to within reasonable accuracy, we applied a linear fit to the latter plot.

Figure 6.17 A sketch of the density change versus the simultaneously measured temperature change during local heating.

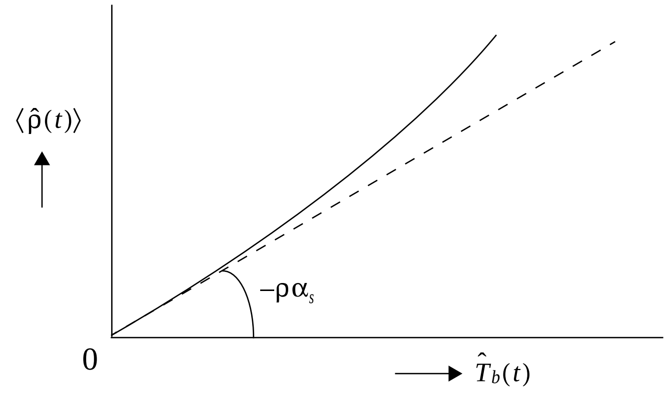

6.5.2 Results and discussion

From the body of available experimental data altogether 15 useful runs were obtained. For these runs, data for determination of c_v were obtained from the response of the sample to changes in T_{set}. Clearly, it would have been preferable to use the gold layer heater to generate the PE required for c_v measurement. However, for the measurement of D_T, the PE has to be kept small. Therefore, the D_T measurements cannot be used to determine c_v. In selecting the useful runs, it was found that some were disturbed by gravity jitter or the $\hat{T}_b(t)$-profile was too irregular to adhere to the theoretical model as discussed in section 2.3. The results of the measurements of $-\rho\alpha_s$ along the critical isochore are summarized in table 6.3. This table consists of the temperature difference with T_c at which the measurement was performed, the way in which T_{set} was changed (see section 3.1.5), referred to as thermal disturbance, and the resulting $-\rho\alpha_s$ including its accuracy. The accuracies are standard deviations which are produced by the fitting program (Igor Pro by WaveMetrics, Inc.).

Table 6.3 Measured values of ($-\rho\alpha_s$).

nr.	$T - T_c$ (mK)	thermal disturbance	$-\rho\alpha_s$ (kg m^{-3} K^{-1})
1	2468	step to 1 K	18.4±0.3
2	2468	step to 2 K	19.4±0.3
3	2000	step to 1.5 K	19.7±0.6
4	1500	step to 0.8 K	21.0±0.5
5	1025	step to 325 mK	21.1±0.2
6	660	step to 468 mK	21.1±0.2
7	450	ramp of 250 mK/hr	22.7±0.4
8	325	step to 100 mK	24.3±0.4
9	168	step to 150 mK	27.0±0.4
10	150	ramp of -100 mK/hr	23.9±0.8
11	125	step to 45 mK	26.2±0.2
12	106	step to 100 mK	25.9±0.8
13	50	ramp of -20 mK/hr	26.2±0.2
14	30	ramp of -40 mK/hr	29.7±0.7
15	5	ramp of 95 mK/hr	32.3±1.4

It must be reminded here that true equilibrium of the fluid was never reached, as pointed out in section 6.1.1, before the fluid was thermally disturbed. The residual drift in the density in a ‘quasi steady state’ was unimportant for D_T measurement, since it could be neglected in comparison to the relatively large density changes in boundary layers (related to α_p) following local heating. However, for c_v measurement this drift is important since to the relatively small isentropic density changes in the bulk it is often significant. This drift results from the late stage of equilibration and is completely additive to the bulk density changes due to the PE. Therefore, in order to separate the two effects during the thermal disturbance, we employed a baseline correction based on an extrapolation of the pre-disturbance behaviour of the fluid. However, it is unclear to what extent this baseline correction may account for the behaviour of the boundary layers along the optical path. At this point an impression of the inaccuracies of this baseline subtraction may be obtained from the scatter in the results.

In fig. 6.18 examples are shown of simultaneous measurements of the PE-induced temperature and density changes during a thermal disturbance, as determined by the abovementioned procedure (after baseline correction). In this figure the density changes are represented by the interference order changes. It shows that the density and the temperature respond in a similar way to a disturbance, as is to be expected by the mechanism of the PE. Note that interference order and temperature are measured in different positions in the fluid, but outside the boundary layers. Most prominently the similar response is displayed for runs 5 and 8 in which fluctuations in the heating power give rise to the wavelike modulation in both the temperature and the density measurements. As expected, all displayed runs in this figure exhibit a thermal lag. Interestingly, for run 15, the increase in density seems to fall behind the increase in temperature after some 200 seconds of heating. This can be explained by a noticeable decrease in $-\rho\alpha_s$ as, for this run, the temperature difference to T_c is increased relatively large. A fit of Mt^{μ} to the $\hat{T}_b(t)$-profiles, in order to determine $I(\mu)$, yielded values of μ between 1 and 2. The subsequent determination of $E(\tau)$ through eq.(6.10) was done with the aid of the equation of state (EOS) developed by Wyczalkowska, Das and Sengers [81]. We notice that at this point, considering that $E(\tau)$ appears just in a correction term, it is sufficient to turn to an EOS instead of trying to incorporate extrapolations of (scarcely available) experimental data.

Figure 6.18 Measurements of bulk temperature and density changes.

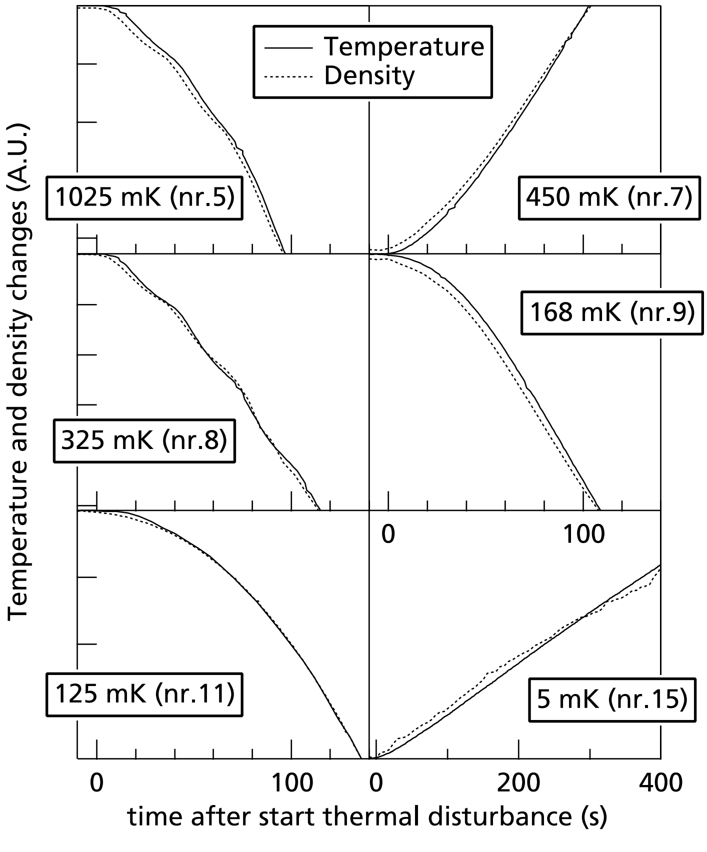

In fig.6.19, a typical example is given of $\langle\hat{\rho}(t)\rangle$, converted from the measured order changes according to eq.(5.5), displayed versus $\hat{T}_b(t)(1+E\sqrt{t})$. Ideally, in agreement with eq.(6.9), this should result in a straight line through the origin. However, in practise, both for small values as for large values a deviation from this line to lower values is seen (although barely visible in this plot).

The small values correspond to small times at which a simple time shift (thermal lag correction) to the temperature data (as mentioned in the previous section) does not provide an accurate correction to the effect of the response time of the thermistor, t_r. The deviation at large values, corresponding to large times, is expected when after a time t_d one of the developing boundary layers will reach a position at which either $\hat{T}_b(t)$ or $\langle\hat{\rho}(t)\rangle$ is observed. In that case, the temperature measurement will be higher or the density measurement will be lower. Therefore, the linear fit through this plot is restricted to times t for which $3t_r < t < t_d$. Both time limits are indicated in fig. 6.19 by dashed squares.

Figure 6.19 A plot of <ρ(t)> versus $T_b(t)(1+E\sqrt{t})$.

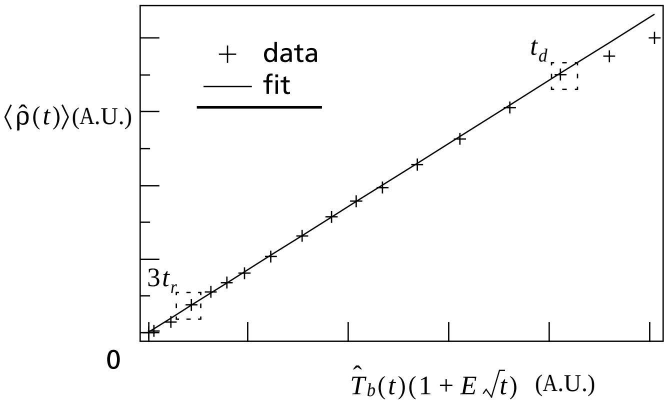

The values of $-\rho\alpha_s$ are converted on the basis of eq.(6.7) to values of c_v. In this conversion, T_c (necessary since we know only $T-T_c$) and $(\partial p/\partial T)_\rho$ are taken from the scaled crossover EOS by Wyczalkowska, Das and Sengers [81]. The uncertainty in these values is much smaller than the experimental accuracy in the determination of $-\rho\alpha_s$. For ρ we use our own measured value ρ_c (see chapter 5). In fig. 6.20 the measured values of c_v are displayed together with earth-based results by Straub and Nitsche [97], which are represented by a power law relation, and the values given by the EOS. It shows that our results are in good agreement with the EOS but are smaller than the experimental values by Straub and Nitsche [97]. More recent, microgravity measurements by Straub, Haupt and Eicher [98] reveal values for c_v in line with the EOS and, therefore, also in agreement with our results. The evaluation of these measurements by Haupt and Straub [99] in a region close to T_c has resulted in a power law relation which is displayed also in fig. 6.20. It shows that in this region more measurements by the present method are necessary in order to compare effectively the results by the two methods.

Figure 6.20 A double logarithmic plot of c_V versus $T\text{-}T_c$.

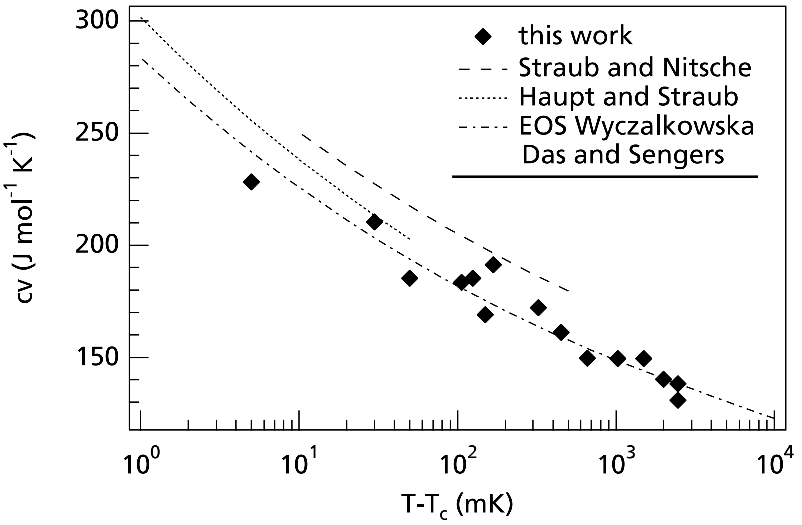

In accordance to the expected asymptotic behaviour (see section 2.1.2), in the measured temperature range, c_V can be represented in terms of a simple power law (see eq.(2.10)) with added to it a temperature independent background term, as suggested by the renormalization-group method [15,43,44]. Using the universal value for α (=0.11), a fit to the present data results in

$$\frac{c_V}{R} = 326(\pm25)\cdot\tau^{-0.11} + 234(\pm58)\,, \tag{6.11}$$

where R is the gas constant. Unfortunately, the presently obtained accuracy does not permit an accurate fit through our data that could decide onto the value of the exponent α. The limited accuracy must be attributed to the fact that both the SCU and the experimental scenario were not optimized for this particular investigation, as mentioned in the introduction of this section (6.5). Still, simultaneous measurement of temperature and density changes to obtain $-\rho\alpha_S$ appears to be a particularly convenient way for probing the theory near CP. Clearly, in a possible follow up of this part of the investigation, a great improvement in experimental accuracy may be obtained. The temperature measurement may be improved by using smaller sensors as, generally, this will reduce both the temperature lag and the response time. The accuracy in the density measurement would gain enormously by an improvement in approximate equilibrium before the thermal disturbance is applied. Apart from possible improvements in thermal stability of the THU and SCU, this may be accomplished by longer waiting periods, a smaller volume of the sample and limiting the number of (heat producing) sensors and high thermal impedance elements within the fluid. More accurate knowledge of the influence of the boundary layers in the optical path may be obtained by choosing carefully the heating profile. Finally, this influence may be reduced by a greater distance between the window and mirror, for which materials should be used with the highest possible thermal impedance.

Interestingly, simultaneous measurements of the bulk temperature and density changes show that already small disturbances in the gravity level (gravity jitter) break down the constant, isentropic correspondence between the bulk temperature and density. In fig. 6.21, the time-derivative of the temperature and the density are displayed versus time upon a change in T_{set} from T_c+125 mK to T_c+ 45 mK, together with the corresponding gravity level detected by one of the SAMS gravity sensors inside the space shuttle (the one next to CPF) [101]. Note that the time scales of the two graphs differ by a factor 100! Exactly at the moment a small disturbance in the gravity level (~10^{-4} g) was detected, a reaction was observed of only the density and not the temperature. A comparison between all disturbances of this kind observed by the gravity-level monitor of the space shuttle [101] and the fluid's reaction showed each time the same effect. A possible cause could simply be a disturbance in the measurement geometry, but a decisive explanation of this phenomenon we haven't been able to come up with and new measurements are needed to clarify this issue. Still, we conclude that in the interpretation of PE-data deduced from microgravity experiments, special attention should be paid to gravity jitter.

Figure 6.21 Illustration of the isentropic character of the T-ρ response and its break down due to gravity jitter. The dashed vertical line indicates the start of the gravity jitter. The actual size of the disturbance in the gravity level is displayed in the upper part.

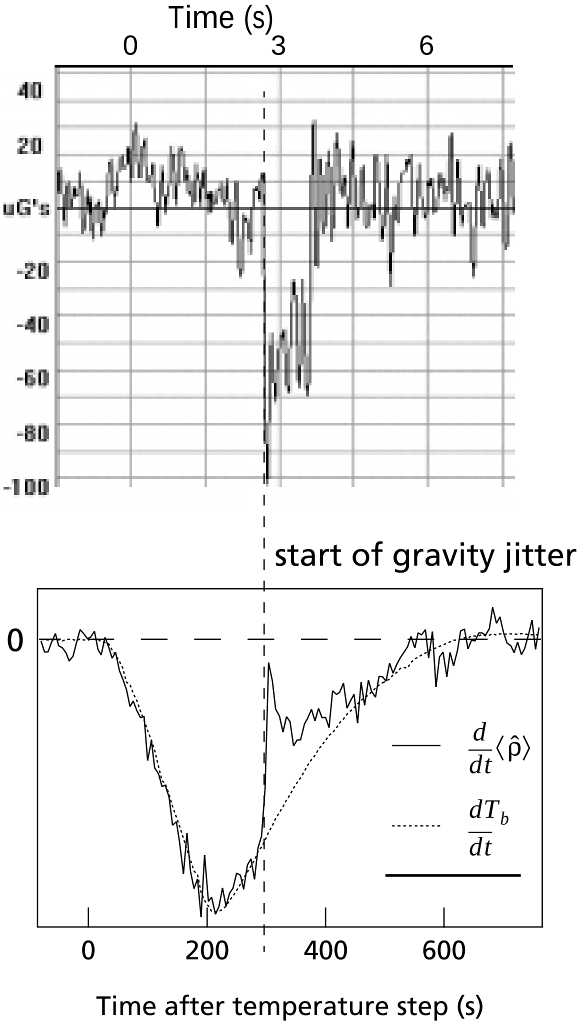

In the earth's gravitational field, applying known methods, the density stratification in the critical region due to the hydrostatic pressure profile distorts the measurement of c_v to an extent that, for SF_6, reliable data much closer to T_c than 50 mK is not to be expected. For a proper assessment of the asymptotic behaviour of c_v, for measurements it is unavoidable to turn to a microgravity environment. With the introduction of the present method, two methods have been utilized to measure c_v in a microgravity environment. The scanning radiation calorimeter with which Straub et al. [98] measured, provided excellent results in agreement with an existing EOS [81]. To confide in this method, the inhomogeneities inevitably introduced by this method were measured and calculated to be relatively small and their influence on the measurement of c_v was calculated to be within 1%. However, although the temperature distribution is measured in this method, no direct measurement of the density distribution is possible. Investigations into critical anomalies show that results are influenced strongly by remaining inhomogeneities in the density and the possibility cannot be excluded that these inhomogeneities are present. In addition, this method hinges on the accuracy with which quantities like the thermal impedance, the heat input, the heat capacity of the container and the mass of the sample can be determined. The present method on the other hand enables the direct observation of both the temperature and the density profile, and in principle depends only on the accuracy with which the relation between the density and the refractive index is known. Furthermore, the present method allows other types of measurements near CP to be performed on the same sample, which is often not unwelcome in a costly and time-limited space experiment. In view of the abovementioned reasons, isentropic thermalization in microgravity provides a necessary, complementary method to accurately determine c_v in the critical region of pure fluids.

6.5.3 Conclusions

A new method to determine the isochoric specific heat in a microgravity environment is developed, based on the occurrence of the PE. Values of c_v are obtained in a range of 5 mK < $T - T_c$ < 2.5 K. The measured values of c_v are in good agreement with both an existing scaled crossover EOS and results from a microgravity experiment, but differ from earth-based measurements. The accuracy was limited because the experiment was not optimized to perform these measurements. Apart from the improvements, based upon theoretical and experimental information in this thesis, that can be employed in future experiments of this kind, it is noted that special attention should be paid to gravity jitter.

Given the difficulty in measuring c_v in the critical region, isentropic thermalization in microgravity provides a necessary, complementary method to accurately determine c_v in the critical region of pure fluids. Moreover, we have shown that simultaneous measurements of temperature and density - in microgravity - offer an excellent tool for assessing the quality of existing equations of state in the near critical region.